Laser and Particle Beams (2001), *19*, 541–556. Printed in the USA.

DOI: 10.1017.S0263034601194036

Wire number breakthrough for high-power annular *z* pinches and some characteristics at high wire number

T.W.L. SANFORD
Sandia National Laboratories, Albuquerque, NM 87185-1196, USA

(Received 22 May 2000; Accepted 13 February 2001)

Abstract

Characteristics of annular wire array *z* pinches as a function of wire number and at high wire number are reviewed. The data, taken primarily using aluminum wires on Saturn, are comprehensive. The experiments have provided important insights into the features of wire-array dynamics critical for high X-ray power generation, and have initiated a renaissance in *z* pinches when high numbers of wires are used. In this regime, for example, radiation environments characteristic of those encountered during the early pulses required for indirect-drive ICF ignition on the NIF have been produced in hohlraums driven by X rays from a *z* pinch, and are commented on here.

1. INTRODUCTION

The discovery (Sanford *et al.*, 1995, 1996*a*, 1996*b*) that the use of very large numbers of wires enabled the generation of high X-ray power from annular wire array *z* pinches represented a breakthrough (Matzen, 1997; Yonas, 1998) in controlling *z*-pinch instabilities. This 1995 discovery was a major step forward in load design for large pulsed-power generators (Quintenz *et al.*, 1996, 1998; Cook, 1997; Mehlhorn, 1997; Ramirez, 1997). Combined with the conversion of the PBFA-II generator to a *z*-pinch driver (Spielman *et al.*, 1996, 1997, 1998), the successful application of this breakthrough on Z (Sanford *et al.*, 1998*b*) reopened interest in the field of fast, dynamic *z* pinches (Ryutov *et al.*, 2000) as X-ray sources for fusion (Matzen, 1999; Matzen *et al.*, 1999), as well as initiated a renewed study of *z* pinches (Haines, 2000) for other high energy-density applications (Matzen, 1997).

At Sandia National Laboratories, for example, three hohlraum concepts that take advantage of the high X-ray powers generated with this new pulsed-power capability are under development to investigate the feasibility of *z* pinches to drive ICF (inertial confinement fusion) targets (Cook *et al.*, 1998; Quintenz *et al.*, 1998; Matzen, 1999; Matzen *et al.*, 1999; Leeper *et al.*, 1999). They are referred to as the *z-pinch driven* (Porter, 1997; Hammer *et al.*, 1999), the *dynamic* (Lash *et al.*, 1999; Nash *et al.*, 1999*a*), and the *static-wall* hohlraums (Olson *et al.*, 1999). To date, the large-volume *z*-pinch driven hohlraum has developed a temperature of 95 ± 5 eV in a 17-mm diameter by 15-mm high hohlraum, when heated by radiation generated external to a single pinch (Cuneo *et al.*, 1999). The energy-efficient dynamic hohlraum, which uses radiation generated internal to a radially converging target heated by the imploding wire array, has developed temperatures ranging from 80 to 180 eV as the diameter of a 10-mm-high hohlraum compresses from 5 to 1.6 mm (Leeper *et al.*, 1999). And the static-wall hohlraum, which combines features from both concepts, has developed a temperature of 130 ± 7 eV in a NIF (National Ignition Facility)-scale (6-mm diameter by 7-mm high) hohlraum (Sanford *et al.*, 1999*d*), again when heated by X rays from a single pinch (Fig. 15B to be discussed in Sect. 4).

The breakthrough experiments (Sanford *et al.*, 1995, 1996*a*, 1996*b*) were done on the 10-MA Saturn generator (Bloomquist *et al.*, 1987) with aluminum wires, where the wire number varied from 10 (or 13) to 136 (or 192) for 8.6 mm (or 12 mm) radii array loads, respectively (Fig. 1). At each radius (8.6 or 12 mm), the total mass was held constant (0.66 or 0.82 mg, respectively). Analyses of these experiments showed that a key parameter controlling the X-ray power emitted at stagnation was the interwire gap spacing. Decreasing the interwire gap from 6 to 0.4 mm (the limit of load construction capability) increased the total power by a factor of ~20 and the total energy by ~2, for either array radius. A dramatic increase in X-ray power occurred when the interwire gap spacing decreased below ~2 mm (Fig. 2). The onset of this rapid rise in power correlated with simultaneous discontinuities in the rate of change in other measurable quantities such as radiated pulse width (Fig. 3A), radial pinch convergence (Fig. 3B), total radiated

Address correspondence and reprint requests to: T.W.L. Sanford, Sandia National Laboratories, MS-1196, Organization 1677, P.O. Box 5800, Albuquerque, NM 87185, USA. E-mail: twsanfo@sandia.gov

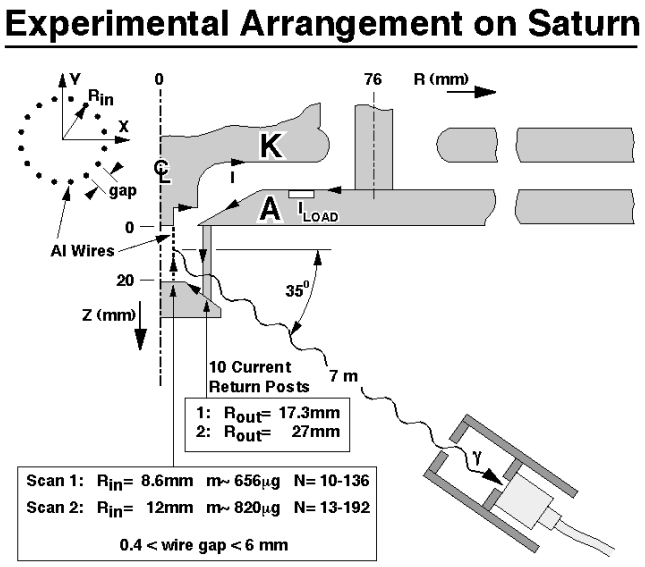

Fig. 1. Schematic cross section of 1995 Saturn experiment.

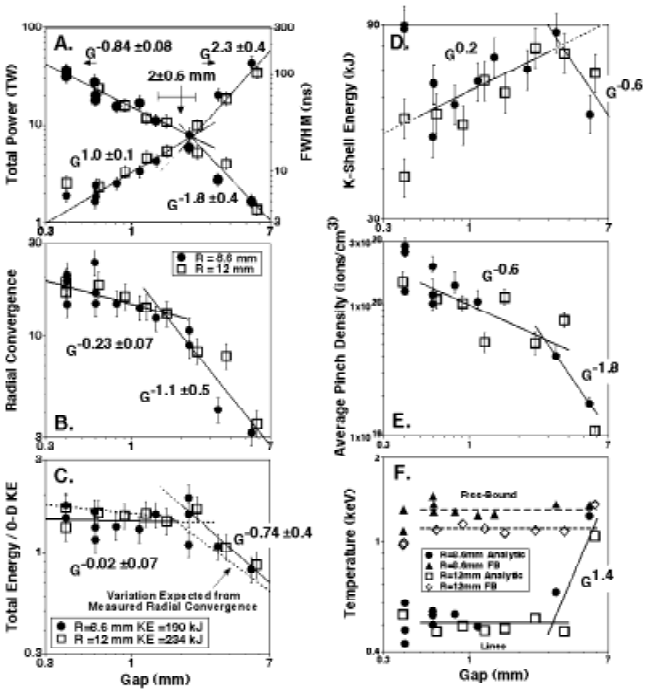

Fig. 3. (A) Peak total radiated power (solid line) and pulsewidth (dashed line), (B) radial convergence, (C) total radiated energy normalized by calculated kinetic energy assuming a 10:1 convergence, (D) *K*-shell energy (8.6-mm data are scaled by 1.23), (E) average ion densities inferred from time-integrated *K*-shell spectra, (F) average electron temperature (lines) inferred from time-integrated *K*-shell spectra and electron temperature (free-bound) inferred from measured free-bound continuum slope at time of peak power. ● and □ correspond to the 8.6-mm (small-radius) and 12-mm (large-radius) data, repectively.

energy (Fig. 3C), *K*-shell energy (Fig. 3D), pinch density (Fig. 3E), pinch temperature from *K*-shell emission (Fig. 3F), and instability observations (Fig. 4). The discontinuity in the Figure 3 data correlated with a calculated 2-D transition from the implosion of individual self-pinching *wire plasmas* to that of a *plasma shell* having azimuthal variations that diminished with increased wire number (Sanford *et al.*, 1996*a*, 1996*b*). In this calculated plasma-shell regime, many features of the data were consistent with RMHC (radiation-magneto-hydrodynamic code) simulations (Hammer *et al.*, 1996; Peterson *et al.*, 1996) that take into account the development of the magnetically driven R-T (Rayleigh–Taylor) instability in the *r*–*z* plane, assuming an azimuthally symmetric plasma shell. The use of large wire numbers reduced the azimuthal asymmetry of the initial plasma, improved the shot-to-shot repeatability, and thus permitted, for the first time, details of wire array implosions to be meaningfully compared with such 2-D simulations over the full span of X-ray emission (Sanford *et al.*, 1997*c*). Moreover, 1-D simulations which accounted for the finite shell thickness through the use of viscosity and conductivity multipliers could now be used to extract relevant parameters of the pinch at stagnation (Whitney *et al.*, 1997).

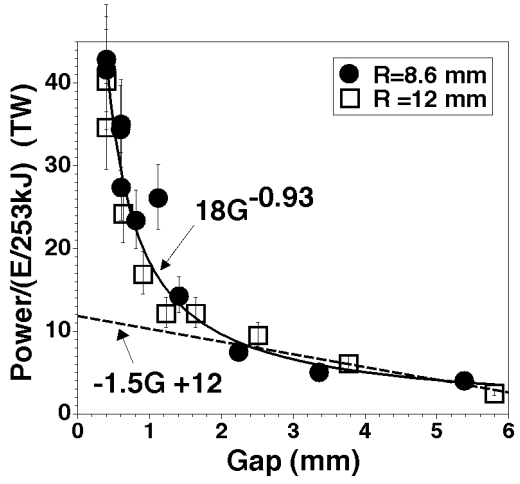

Fig. 2. Total radiated power normalized by the total radiated energy (scaled such that the normalized power agrees with that measured at the smallest gap) versus initial interwire gap.

Previous experiments using wire array *z*-pinch loads did not show significant improvement in performance when the wire number increased beyond 10–20 wires (Pereira & Davis, 1988; Ramirez, 1997). Twenty-four wires were generally considered adequate to provide sufficient azimuthal symmetry for *z*-pinch loads. Such loads (Spielman *et al.*, 1993) were routinely used for radiation-effects studies at Sandia. These loads developed unstable axial pinches that exhibited poor reproducibility, and research was accordingly directed to developing implosions of the more azimuthally symmetric annular and solid gas-puffs loads (see papers in Pereira *et al.*, 1989 and Haines & Knight, 1993). In early 1995 when bringing into operation a fast-framing pinhole camera (Ruggles *et al.*, 1995) to examine the early implosion phase of a typical 24-wire aluminum array on Saturn,

https://doi.org/10.1017/S0263034601194036 Published online by Cambridge University Press

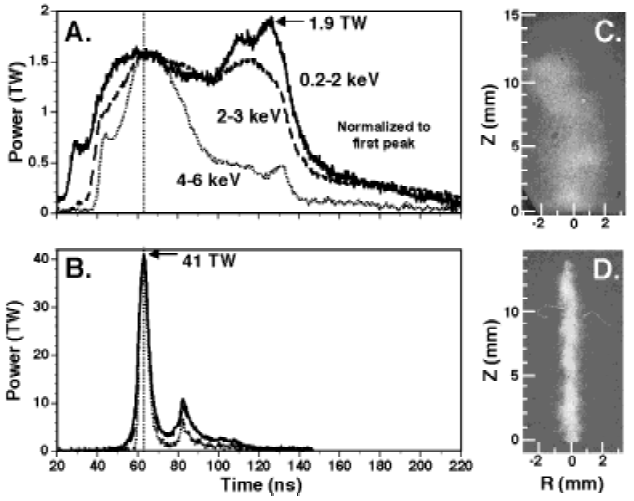

Fig. 4. Radiation pulseshapes in three energy channels normalized to the peak power measured in the lowest energy channel for the large-radius array where (A) $G = 5.5$ mm and (B) $G = 0.4$ mm. Time is measured from a linear extrapolation of the leading edge of the main current pulse to the abscissa. (C) and (D) are associated time-integrated X-ray images, respectively.

however, self-pinching of the individual wires was clearly observed prior to the implosion of the array (see Figs. 7–9 in Sanford *et al.*, 1999*a* and Fig. 7 to be discussed in Sect. 2.2). This measured lack of a coherent plasma shell prior to the radial implosion of the array motivated the use of increased wire number. The data suggested that perhaps these unstable pinches could be better stabilized if more wires were added in order to eliminate the self-pinching by the formation of a continuous plasma shell prior to array implosion (Sanford *et al.*, 1995).

This article reviews the experimental and theoretical understanding generated by the 1995 wire-number variation experiment (Sanford *et al.*, 1995, 1996*a*, 1996*b*, 1997*a*, 1997*c*, 1999*a*; Whitney *et al.*, 1997; Nash *et al.*, 1998) and characteristics measured in follow-on experiments in 1996 at high wire number (Sanford *et al.*, 1998*c*, 1998*d*). Since other limited summaries of these data have been published (Sanford *et al.*, 1997*b*, 1998*a*, 1999*b*), features measured in the very high number wire regime for the first time are highlighted and integrated into a coherent picture. Subsequent measurements made with tungsten wires on Saturn (Deeney *et al.*, 1997) and Z (Sanford *et al.*, 1998*b*) confirm the general increase in X-ray power with wire number. Discussion of these measurements is deferred to the original references.

Since the discovery, a considerable amount of research has been done to understand the dynamics of fast *z* pinches (Haines, 2000; Ryutov *et al.*, 2000). The Heuristic Model of Haines (1998), the numerical simulations of Chittenden *et al.* (1999, 2000), and the measurements of Lebedev *et al.* (1998, 1999, 2000) and Sinars *et al.* (2000, 2001) have significantly aided in elucidating the Saturn experiments. In this review article, the insights from this research are incorporated into the discussion. Measurements made with one of the hohlraum concepts (Olson *et al.*, 1999) (and that which the author has been associated with) are used as an example of what has been achieved to heat ICF-relevant hohlraums (Kilkenney *et al.*, 1999) to high temperatures in the high wire number regime with tungsten wires on Z. Of relevance to this review, examination of the axial radiation driving this hohlraum configuration measured with an axial diagnostic package (Hurst *et al.*, 1999; Nash *et al.*, 1999*b*) shows that the addition of a low-density foam target on axis can reduce the effective size of the radial pinch by a factor of 2, creating ~3-ns-wide radiation pulses when viewed from the side. The size reduction permitted cylindrical hohlraums of ICF-relevant dimensions (4-mm diameter by 4-mm height) to be driven to the high temperature of 155 ± 8 eV in a *z* pinch (Sanford *et al.*, 1999*c*, 2000*a*, 2000*b*). Measurements made with this geometry suggest the presence of an azimuthal mode number in the axial emission for the first time in high-wire-number implosions that utilize a solid current-return can (Sanford & Roderick, 2001).

2. WIRE NUMBER VARIATION

2.1. Experimental Observations

2.1.1. Emission characteristics

As summarized in the introduction, decreasing the inter-wire gap in the 1995 experiments resulted in monotonic increases in total radiated power (Fig. 3A) and energy (Fig. 3C), and simultaneous decreases in the width of the X-ray pulse (Fig. 3A), similarly for both array radii. For gaps smaller than 2 ± 0.6 mm, the character of the X-ray emission qualitatively changed, from a broad, irregular radiation pulse at large gaps (Fig. 4A) to a narrow, evenly shaped radiation pulse followed by a much weaker pulse at small gaps (Fig. 4B). The weaker second radiation peak in Figure 4B is consistent with a second radial implosion and corresponds to a pinch having a lower temperature relative to that of the first implosion (Sect. 3). For gaps greater than ~2 mm, time-integrated images of the pinch (mainly showing the plasma at stagnation) exhibit the presence of kink ($m = 1$) as well as sausage ($m = 0$) instability (Fig. 4C). Time-dependent images show significant precursor plasma stagnating on axis, generating soft X-ray emission tens of nanoseconds prior to the main implosion, in agreement with earlier and current (Lebedev *et al.*, 1998, 1999, 2000) experiments. For gaps less than ~2 mm, in contrast, no kink instability occurs and only minimal precursor plasma forms (Fig. 4D). The changes in the temporal shape of the X-ray pulse (Fig. 4A, 4B) and in the spatial quality of the pinch (Fig. 4C, 4D) with gap occurred with corresponding quantitative transitions in the rates of change of the peak total X-ray power and its pulsewidth (Fig. 3A), the radial convergence (obtained from the average size of the *K*-shell

https://doi.org/10.1017/S0263034601194036 Published online by Cambridge University Press

emission region; Fig. 3B), the emitted total X-ray energy (Fig. 3C), the emitted *K*-shell energy (Fig. 3D), and other measured X-ray characteristics above and below a gap of ~2 mm (Sanford *et al.*, 1999*a*). Not enough data were taken at wide gap spacings, however, to ascertain how sharply this transition in X-ray behavior took place. For this reason, it is represented simply as a transition between two gap-dependent power laws as illustrated in Figure 3, with the gap (G) exponents indicated.

In general, variations in the peak total power track the inverse of the measured pulsewidths (Fig. 3A), as would be expected if the total energy radiated during stagnation is slowly varying. The greater rate of dependence on gap of the pulsewidth and the peak power, for gaps greater than ~2 mm, reflects the greater disorganization of the implosion as seen by the lost double-pulse nature of the stagnation (Fig. 4A, 4B). The increased rate of decrease in power for large gaps relative to that for small gaps is consistent with the decrease in total radiated energy (Fig. 1D in Sanford *et al.*, 1999*b*). This change in energy is approximately consistent with the change in the calculated kinetic energy (dotted lines in Fig. 3C) (and by inference the radiated energy), using the measured radial compression from the *K*-shell emission images (Fig. 3B). The larger-radius load permitted the delivery of ~23% more kinetic energy to the load for a fixed radial convergence of 10. In Figure 3C, the measured total radiated energy is normalized to the calculated 0-D kinetic energy, and increasing the kinetic energy of the smaller-radius load by 23% produces the universal curves of Figures 3C and 3D, respectively. Normalizing the peak total radiated power by the total radiated energy (and scaling the results to the average of the peak power measured at the smallest gap measured) generates the universal curve of Figure 2. In this form, the normalized power P could also be described by a simple inverse gap G scaling over the entire range measured: $P\ (\mathrm{TW}) \sim 18 * G\ (\mathrm{mm})^{-0.93\pm0.1}$ (Sanford *et al.*, 1998*a*, 1999*a*). An associated gap scaling was also observed in the measured risetime for all X-ray channels examined (Fig. 14 in Sanford *et al.*, 1999*a*).

2.1.2. Pinch characteristics

Measurement of the slope of the optically thin, free-to-bound, X-ray emission determined the electron temperature of the hot core of the pinch (Sanford *et al.*, 1997*a* and Sect. 3). This temperature exhibited no variation with gap (dashed lines) and was only a function of the implosion kinematics (Fig. 3F). For large gaps, where the measured ion density was low (Fig. 3E), the temperature (solid lines) extracted from aluminum *K*-shell line ratios (Whitney *et al.*, 1997) agreed with that extracted from the free-to-bound emission. As the gap decreased and the emitting ion density increased (Fig. 3D), however, the optical depth of the *K*-shell emission becomes significant, and the line ratio began to reflect the temperature on the outside surface of the emitting region, rather than an average over the region. The related *K*-shell yield was also suppressed as the ion density and corresponding opacity increased (Fig. 3D). The data taken at the smallest gap (0.4 mm) were generated from wires containing ~5% magnesium. Spectral analyses indicated that >15% of the yield was due to the smaller magnesium mass fraction, and the statistically higher yield in the small-radius load was due to reduced opacity for this element. The transition from a thin to thick plasma, as suggested by the data of Figures 3D–3F, also approximately coincided with the previously discussed transition at ~2 mm (Figs. 2 and 3A–3C).

The difference between the core and surface temperature was indicative of a substantial temperature gradient within the emitting plasma (Fig. 3F). Remarkably, the enhanced plasma density at small gaps increased the temperature and density gradients and opacity effects, in such a way as to approximately maintain the average amount of mass participating in the *K*-shell emission at 11 ± 3%, independent of gap. These density and temperature measurements showed that the increase in *K*-shell power measured (and by inference the total power) was the result of systematically greater plasma compression (Fig. 3E) and was not the result of an increase in temperature (Fig. 3F). (See also the recent analysis of Whitney *et al.*, 2001.)

2.2. Interpretation

2.2.1. Initial simulations

The apparent transition in X-ray emission and inferred pinch characteristics near the 2-mm gap was interpreted using the 2D-TIP RMHC (Marder, 1973; Marder *et al.*, 1998) in *x–y* geometry, using 1D-RMHC simulations of individual wire explosions from a cold start as input (Sanford *et al.*, 1996*a*, 1996*b*). Calculations performed with these codes showed (in correspondence with the experimental data) that a change in the implosion topology occurred with increasing wire number. The calculated implosion made a transition from one topology composed of non-merging, self-pinching, individual wire plasmas to one characterized by the early formation and subsequent implosion of a plasma shell. The shell had density and current variations distributed azimuthally that correlated with the initial wire location and which decreased in amplitude with decreasing gap. For the resistivity model employed and for the measured current prepulse and wire sizes fielded, this transition was calculated to occur between wire numbers 20 and 80 (or between interwire gaps of about 3 to 1 mm, respectively) for the small-radius load. For wire number (N) greater than 80, the calculated individual wire plasmas never self-pinched, because the current per wire was too low. For N less than ~20, the current per wire was high enough that the calculated individual wire plasmas always self-pinched in 1-D before stagnation occurred. For $N \sim 40$ (interwire gap ~1.4 mm), the calculated wire plasmas in both 1-D and 2-D partially merged prior to significant radial motion of the array. In general, the TIP *x–y* simulations suggested that the character of single wire plasmas calculated in 1-D provided a qualitative indicator of the behavior of a wire plasma

https://doi.org/10.1017/S0263034601194036 Published online by Cambridge University Press

within an array, with regard to self-pinching or not in the *x–y* plane.

2.2.2. Recent simulations

These 1-D and 2-D simulations have been recently redone using an improved resistivity MHD model (Chittenden *et al.*, 1997, 1999, 2000), called here MHD. In contrast to the earlier calculations, the newer ones indicate that the wire cores remain colder longer, with a greater fraction of the current flowing in the exterior low-density plasma (corona) before implosion occurs, in agreement with MAGPIE (Mitchel *et al.*, 1996) experiments. Figure 5 plots the associated MHD electron-number density calculated in 1-D at a radius of $G/2$ as a function of time (for such single-wire plasmas), assuming that the wire would be an element of the small-radius, 16, 24, 48, 64, or 136 wire arrays on Saturn (Sanford *et al.*, 1999*b*). Throughout the current prepulse (approximately a linear ramp from 0 to 100 kA in 100 ns prior to the main pulse), the density increases in all the wire number configurations. The rapid increase in density at 0 ns is associated with the onset of the main current pulse. As in the earlier 1-D simulations, for the higher wire number configurations ($N \geq 64$) the magnetic field is too weak to cause self-pinching of the individual wire plasma, and the density continues to increase (Fig. 5A). For the lower wire number configuration ($N \leq 48$), the density continues to rise and then falls, as the wire plasma is swept up by the stronger field and then is returned to the wire axis (Fig. 5B). The transition between self-pinching and continued expansion in

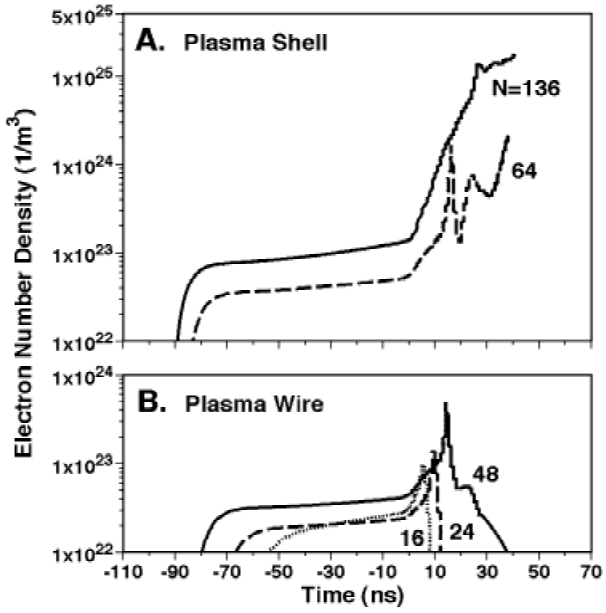

Fig. 5. MHD electron-number density as a function of time at a radius corresponding to $G/2$, for an equivalent wire in a wire array having (A) 64 15-μm, and 136 10-μm diameter wires in the plasma-shell regime, and (B) 16 30-μm, 24 25-μm, 48 17.5-μm diameter wire in the plasma-wire regime, all for the small-radius array. Zero time corresponds to the start of the main current pulse.

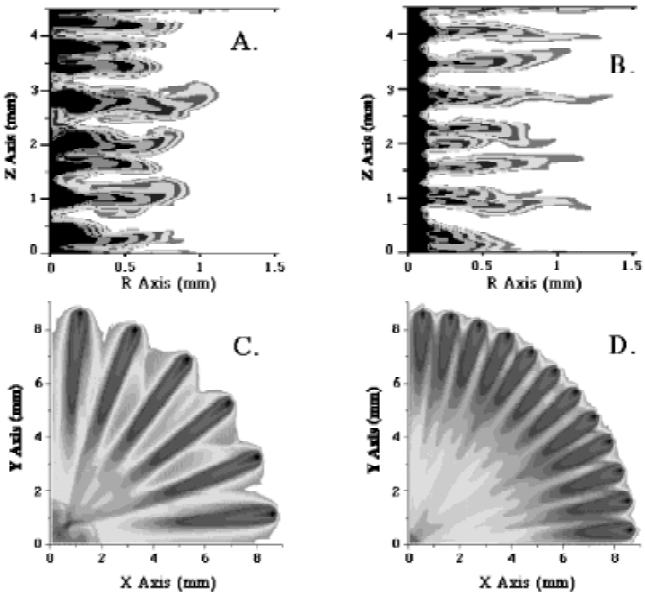

Fig. 6. MHD mass-density log contours calculated in the *r–z* plane for a single aluminum wire, 30 ns into the main current pulse (A) for 1 of 24 25-μm wires and (B) for 1 of 64 15-μm wires, in the small-radius array. MHD mass-density log contours calculated in the *x–y* plane, 35 ns into the main current pulse (D) for 16 30-μm wire, and (E) a 48, 17.5-μm wire small-radius array.

1-D thus occurs between ~48 and ~64 wires. It is qualitatively consistent with the earlier simulations, and with simulations using Trac-II (Reisman, 1998) and ALEGRA (Morse & Carroll, 2000). The general agreement suggests that the breakpoint in topology as calculated in 1-D is somewhat insensitive to the details of the particular resistivity model used (within the granularity of the wire numbers simulated).

Two-dimensional MHD simulations (Chittenden *et al.*, 2000) in the *r–z* plane of a single wire (from a cold start) modify these results slightly, as shown in Figures 6A and 6B for one of 24 wires and one of 64 wires, again for the small-radius load, 30 ns into the main current pulse. Such simulations show that the self-pinching occurs only in the necks of instabilities, and that the remainder of the corona hardly pinches at all. The sausage instabilities set in just when in 1-D the magnetic field would be large enough to pinch the coronal plasma. As a result, there is continued expansion of the plasma in the bulges, while pinching occurs primarily in the necks, as shown by Beg *et al.* (1997) in single-wire experiments. Importantly, these 2-D simulations show that due to the higher current per wire for wires in a lower wire number array, the instability development is greater, which leads to more self-pinching that in turn exacerbates the sausage development. In this case, the instability can reach sufficient nonlinear development that the wire core is penetrated (Fig. 6A) prior to implosion. Because at the start of the implosion the majority of the mass remains in the wire cores, there is a substantial difference in the amplitude of the sausage perturbation between the arrays in which the instability occurs only in the corona (Fig. 6B) compared

https://doi.org/10.1017/S0263034601194036 Published online by Cambridge University Press

to arrays where the instability penetrates the core (Fig. 6A). In the MHD simulations, the transition in perturbation amplitude occurs between 32 and 48 wires (or between inter-gap spacings of 1.7 and 1.1 mm, respectively), and may help explain the difference in gap dependence between the two regimes (Chittenden *et al.*, 2000).

Using MHD, Figures 6C and 6D illustrate the modification to the single-wire density distributions, now in the *x–y* plane, 41 ns into the main current pulse when the wires are placed in an annulus, for 16- and 48-wire arrays, respectively. In MHD, again cold solid wires were used as the initial conditions. Both configurations exhibited the low-density corona being swept around the dense cores by the global magnetic field, which streams toward the axis (jetting), forming a precursor plasma stagnating on axis. With the 16-wire array, the plasmas have self-pinched, in agreement with the single-wire simulations. With the 48-wire array, the low-density regions have merged, but the higher-density regions still retain the characteristically teardrop-shaped azimuthal asymmetry, again in qualitative agreement with the 1-D simulations. The global field distorts the otherwise symmetrical expansion of the wire plasma into the characteristic tear-rop shape shown. Because hotter individual-wire plasma was calculated in the 1-D simulations used as input to TIP, the initial TIP simulations (Sanford *et al.*, 1996*a*, 1996*b*; Marder *et al.*, 1998) did not exhibit the teardrop shape now calculated. The precursor plasma is now more pronounced, owing to the deeper radial penetration of the global magnetic field between wires with decreased wire number.

The initial and more recent calculations of the transition are seen to be consistent with the motivating images mentioned in the introduction, where loads having gaps of 1.3 mm in the now-recognized transition region were recorded. Radial lineouts of some of these images are illustrated in Figure 7A, together with an image (Fig. 7B) taken 19 ns prior to peak radiated power (Fig. 7C). In Figure 7B, for example, individual wire plasmas were observed to neck-off in the form of bright spots (similar to Mosher & Colombant, 1992; Beg *et al.*, 1997; Ruiz-Camacho *et al.*, 1999, and Fig. 6A), and were suggestive of a sausage instability occurring in the individual wires 19 ns prior to peak radiated power. At this time, the calculated radius of the array had only imploded a fraction of a millimeter (as shown by the dashed curve in Fig. 7A). Ten nanoseconds later, after the array radius had imploded an additional 1.5 mm, the observed plasma emission became a continuous distribution, with no evidence of individual wire structure, suggestive of plasma merger (Fig. 7A). At times earlier than 21 ns, the images indicated the presence of a diffuse plasma stagnating on axis, as illustrated in the top lineout of Figure 7A. This plasma may be associated with the precursor plasma calculated in the *x–y* simulations of Chittenden *et al.* (2000) (Fig. 6C, 6D), which arises from the sweeping in of the corona produced from the ablation of the exploding-wire surface by the global magnetic field.

For descriptive purposes, the small-wire-number region where the gap is greater than 2 mm was thus referred to as the *wire-plasma* regime, and the high-wire-number region where the gap was less than 2 mm was called the *plasma-shell* regime, though significant azimuthal density variations within the shell could still exist in this regime. Direct evidence for such a transition in array-plasma character has recently been observed with aluminum wire arrays (Lebe-

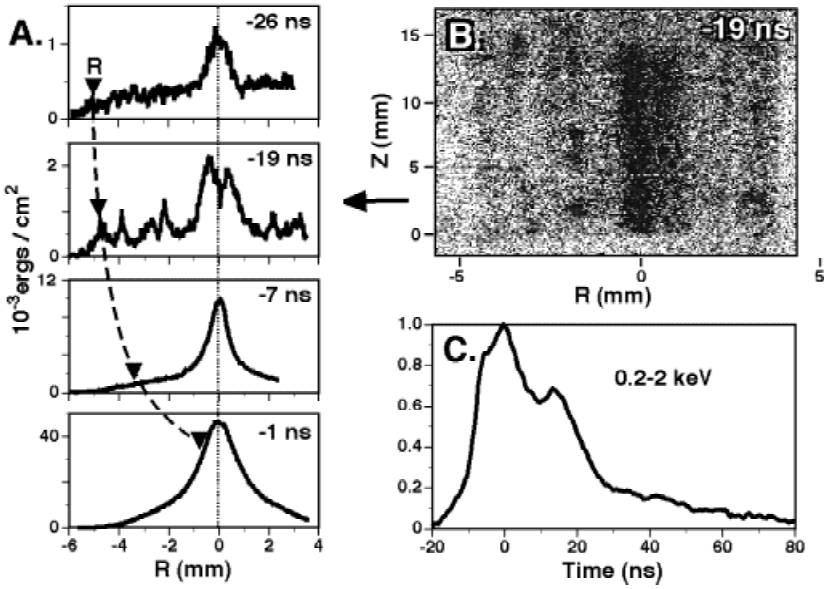

Fig. 7. (A) Lineouts of axially integrated X-ray images as a function of time for a 1.3-mm interwire gap array. (B) Image at −19 ns. (C) Normalized total radiated power pulse. Zero time corresponds to peak radiated power. The wire array geometry was identical to that of the small-radius array, except 24 wires were mounted at a radius of only 5 mm.

https://doi.org/10.1017/S0263034601194036 Published online by Cambridge University Press

dev *et al.*, 2000) on MAGPIE. There, a qualitative change in implosion dynamics occurred when the interwire gap decreased from 1.6 to 0.8 mm. For gaps ≥1.6 mm, the wire cores remained in their initial position until ~80% of the implosion time had elapsed, whereupon they were accelerated to the axis by the sudden transfer of current to the residual cores. During this initial period, current was surmised to flow predominantly in the corona, with the corona continually swept towards the *z* axis by the global magnetic field as in Figures 6C and 6D. In contrast, when the gap decreased from 1.6 to 0.8 mm, the measured array radius accurately tracked that of an 0-D implosion model, which assumed that the array imploded as a hollow plasma cylinder accelerated by the global $\mathbf{J} \times \mathbf{B}$ force.

2.2.3. X–y simulations suggest mechanism for energy dependence

The TIP *x–y* simulations (Marder *et al.*, 1998) together with analytic wire modeling (Mosher, 1994) showed that the wire plasmas (in contrast to the plasma of a shell) may accrue azimuthal velocity components during the implosion owing to deviations in the locations of the individual wires from those of a perfect annulus, wire-to-wire current nonuniformities, or the presence of the limited number of current return posts surrounding the array (Fig. 1), which could seed flute-mode instabilities. These velocity components in a plasma-wire implosion produced increased density asymmetries at stagnation relative to that of a plasma-shell implosion. The resulting difference in the calculated radial convergence between the implosion of a load in the wire-plasma regime relative to that of a load in the plasma-shell regime is illustrated in Figures 8A and 8B, respectively, for a 10-current-return-post geometry as used in the Saturn experiments. In the Figure 8 simulations, the variation in initial wire position arose from numerical noise. Such simulated asymmetries contributed to the reduction in both the compressibility of the stagnating plasma and the resulting radiated energy, both in qualitative agreement with the discontinuity observed in the radial convergence measurements (Fig. 3B) and in the energy channel (Fig. 3C). The increased jetting that also occurs in the wire-plasma regime

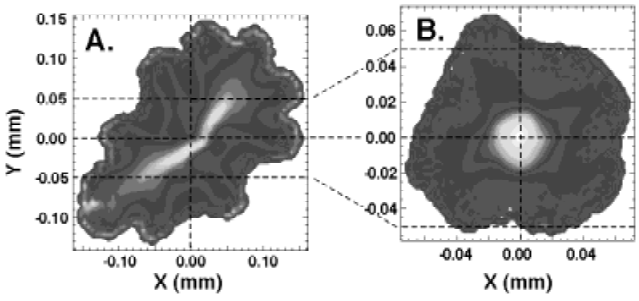

Fig. 8. TIP *x–y* density contours for a small-radius load (having 10 current return posts) at stagnation for (A) a 10-wire array in the plasma-wire regime and (B) a 20-wire array in the plasma-shell regime.

with decreasing wire numbers (Chittenden *et al.*, 2000), with its associated increase in axial plasma that softens the implosion, adds to the decreased convergence and radiated energy resulting from the increased sensitivity to azimuthal asymmetries.

2.2.4. R–z simulations suggest mechanism for power dependence

The TIP simulations showed, however, that the *x–y* variations could not account for the large change in measured pulse shape (Fig. 4A, 4B), for any wire number greater than ~10 or for any reasonable experimental wire or current deviation from azimuthal symmetry (Marder *et al.*, 1998). The effect on the pulsewidth was typically less than a nanosecond. In contrast, RMHC simulations in the *r–z* plane, which assumed an azimuthally symmetric plasma shell with a random density distribution in the *r–z* direction, suggested that the shape of the primary power pulse and the general change in peak power with gap were related to the evolution of the thickness of the plasma sheath due to *r–z* motions and the growth of the R-T instability. This thickness was calculated to scale linearly with the pulsewidth over a limited range (Fig. 22 in Sanford *et al.*, 1999*a*). The measured rise time of the total radiation pulse and the effective pulsewidth (defined as the total energy divided by the peak power—the inverse of the normalized power of Fig. 2) scale as the gap, over the entire gap range explored, showing no discontinuity near 2 mm. This data, together with the simulations, thus suggested a direct relation between the initial interwire gap and the resulting thickness of the imploding sheath (aside from the topology-change effects discussed).

2.2.5. Integrated 3-D model

The Heuristic Model (Haines, 1998) integrates many of the above measured and simulated observations into four-phases: (1) individual wire expansion with sausage-instability development, (2) wire merger to form a conducting shell, (3) continued inward acceleration with R-T instability development in the shell, and (4) pinch formation with equipartition of ion energy to electrons and subsequent radiation. In the model, sausage instabilities in single wires form the seed for the R-T instability in the shell. The level of instabilities reached at the time of merger is greater in arrays of small wire numbers due to the increased current per wire and the longer time before merger occurs. The dependence of implosion quality on gap enters in the thickness of the initial annulus and a reduced average perturbation amplitude for larger wire numbers, in the extent of radial plasma jetting, and in slower energy equipartition between ions and electrons estimated for lower pinch densities. In the model, the geometrical connection between the array radius at which merger occurs and the trajectories of the wire plasmas up to this merger time lead to a nonlinear relation for these parameters and to a division of behavior above and below a critical interwire gap. The critical gap G_c is directly related to the 2-mm transition discussed. For $G > G_c$, the wires

https://doi.org/10.1017/S0263034601194036 Published online by Cambridge University Press

spend the bulk of their implosion time in a wire-plasma regime, and for $G < G_c$, the wire plasmas have merged, forming a plasma shell before significant motion of the array has occurred. For the small-radius Saturn geometry, $G_c = 1.6$ mm. This value is in agreement with the above numerical simulations and measurements. For this small-radius geometry, the model described the measured rise time of the total radiated power pulse as a function of gap when assuming a linear relation between the plasma-shell thickness at stagnation and rise time (Fig. 8B in Sanford *et al.*, 1999*b*).

3. CHARACTERISTICS AT HIGH WIRE NUMBER

3.1. Instabilities and thermogradients measured

The aluminum loads on Saturn in the plasma-shell regime with interwire spacing of less than ~0.6 mm exhibit (Sanford *et al.*, 1997*a*, 1997*b*, 1997*c*) both a strong first and weaker second radiation pulse (Figs. 4B and 9A) that correlate in time with a strong and then weak measured radial convergence (Fig. 9B), hotter and then cooler electron temperatures of the radiating core (Fig. 9C), and higher and then lower ion velocities of the emitting plasma (Fig. 9D), as expected for a double implosion (Mosher, 1989; Whitney *et al.*, 1997). Off-axis images of the X-ray emission and radially resolved X-ray spectra indicate a coherent plasma shell (Fig. 10A) prior to first implosion (stagnation), a converged pinch at stagnation (Fig. 10B) composed of a hot core surrounded by a cooler halo (Sanford *et al.*, 1997*a*; Nash *et al.*, 1998), followed by expanding plasma (Fig. 10C). Images of the X-ray emission from the imploding shell a few nanoseconds prior to stagnation exhibit the classic bubble and spike structure associated with the R-T instability. Axial lineouts at the leading edge of the shell in Figure 10A show, for example, the existence of a 1.1-mm wavelength that merges to form a 3.3-mm wavelength (Fig. 11A). RMHC simulations and Heuristic Model calculations of the wavelength agree with these magnitudes. At stagnation, axial lineouts (integrated over all radii) exhibit only ~10% RMS variations. After stagnation, a clear sausage instability develops (Fig. 11B), whose wavelength appears to be seeded by the long wavelength amplitude of the R-T instability in the prestagnating shell (Fig. 11A). The sausage instability persists into and throughout the next implosion and shows no variation in axial position with time (Sanford *et al.*, 1997*a*).

Figure 9C plots the spatially averaged temperature of the electrons in the core measured from the time-resolved slope of the optically thin free-bound emission and a measure of the electron temperature in the halo from the ratio of the time-resolved, optically thick hydrogen-like to helium-like line emissions. At peak convergence, the temperature of the halo (~0.4 keV) is estimated to be three to four times cooler than that of the core (~1.4 keV), again indicating the presence of strong temperature gradients (see also Fig. 3F at small gaps). While both line and continuum emissions are generated in the hot plasma core at the time of peak convergence, only the optically thin continuum X rays escape the plasma directly. The optically thick line emission is ab-

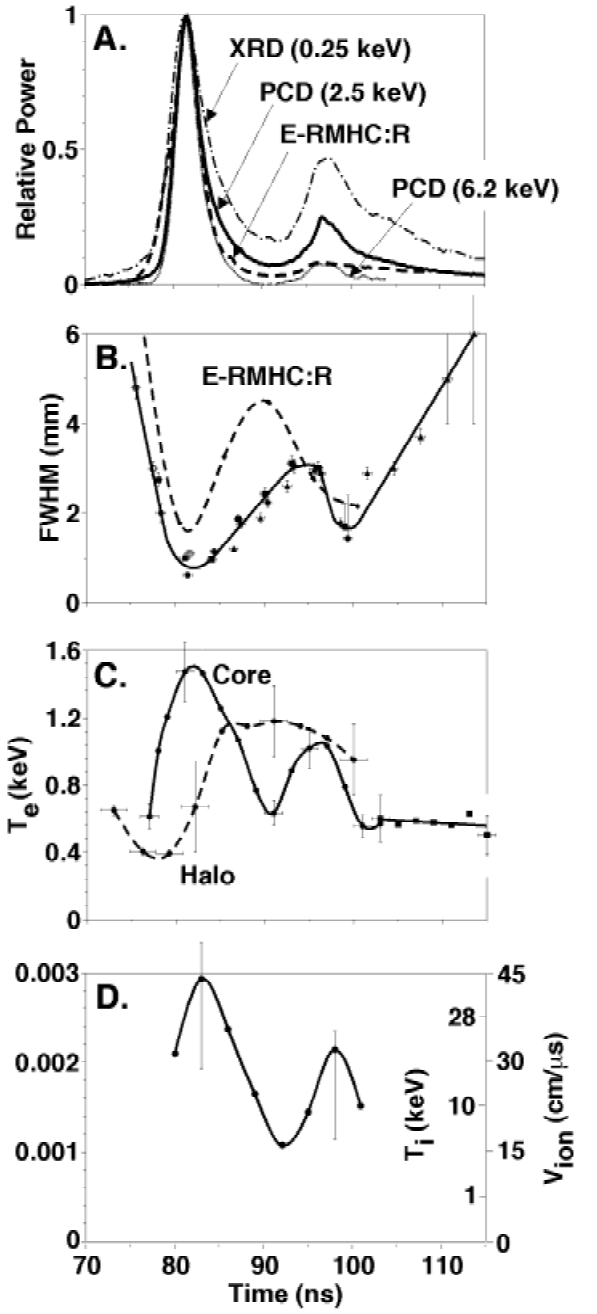

Fig. 9. Measured (A) X-ray power in indicated energy channels (B) diameter of X-ray image radial lineouts averaged over *z* axis, (C) electron core temperature from free-to-bound X-ray continuum and electron halo temperature from the ratio of He-like to H-like transitions, (D) ion velocity from *K*-shell line Doppler shifts, all for the small-radius load having interwire gaps of 0.6 mm. E-RMHC:R simulations of the measured power and diameter are compared in (A) and (B).

https://doi.org/10.1017/S0263034601194036 Published online by Cambridge University Press

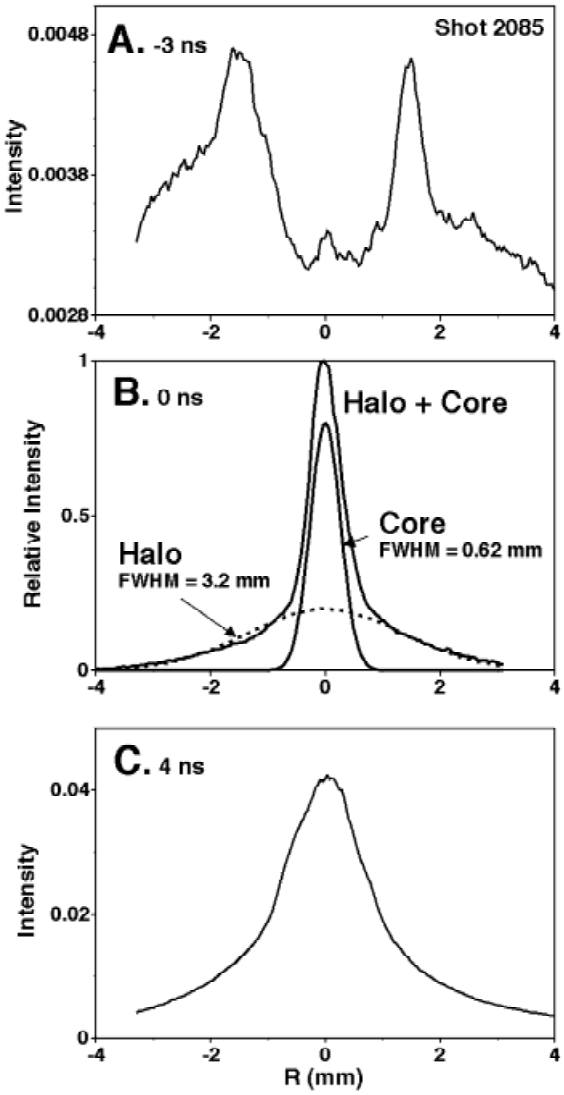

Fig. 10. Radial lineouts integrated over *z* of X-ray images of a 0.6-mm-gap small-radius array taken (A) 3 ns before, (B) at, and (C) 4 ns after peak power.

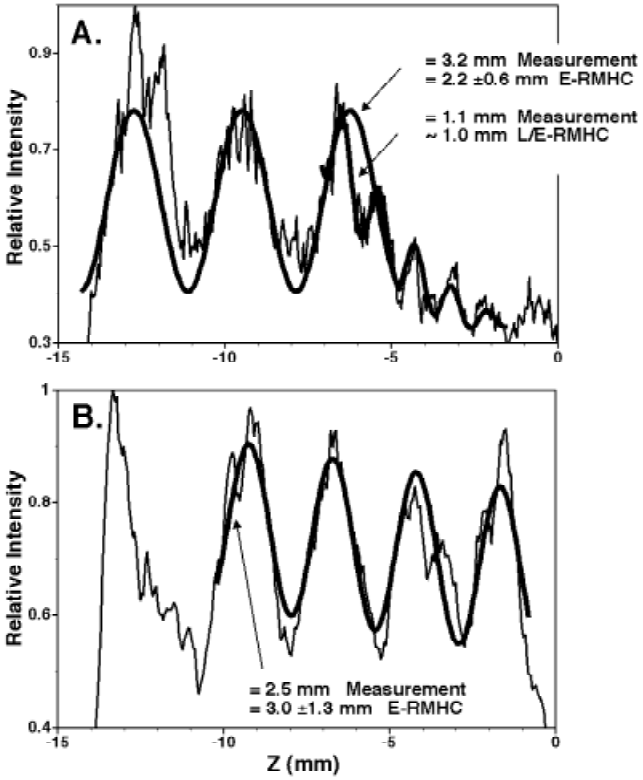

Fig. 11. Axial lineouts of X-ray images of a 0.6-mm-gap small-radius array (A) 3 ns before peak power, at a radius of 1.5 mm (Fig. 10A), and (B) 9 ns after peak power where the lineout is integrated over all radii.

sorbed and re-emitted from the cooler regions until the pinch expands and the plasma opacity declines. The high temperature inferred from the line analysis at times when the plasma is expanding and the core electrons are cooling (Fig. 9C) suggests a lag in recombination (Whitney *et al.*, 1997). That is, the ionization state is likely no longer in equilibrium with the cooled electrons, but reflects instead the earlier state of the plasma when the electrons were hot and the plasma was in equilibrium. The core electrons cool too rapidly in this case for recombination processes to maintain ionization equilibrium.

3.2. 2-D simulations

In general, many of the features measured at the first implosion in this high-wire-number plasma-shell regime agree with RMHC simulations that take into account the dominant R-T instability in the *r*–*z* plane (Sanford *et al.*, 1997*c*). In these 2-D simulations, the magnitude of a random-density seed used to initiate the instability is adjusted so that the width of the radiation pulse generated at stagnation agrees with that measured for a soft-energy channel, such as that shown in Figure 9A (dashed curve) for a three-temperature E (Eulerian)-RMHC (Peterson *et al.*, 1996) simulation. These E-RMHC simulations provide insights into the underlying dynamics for a typical high-wire-number plasma-shell implosion, which are not easily measured. Figure 12A, for example, shows that the mass-averaged radius basically tracks the current-averaged radius up to stagnation, diverging for times beyond peak radiated power. At the minimum mass-averaged radius of ~0.5 mm, E-RMHC indicates a pinched plasma column with a hot high-density core surrounded by a somewhat cooler and slightly lower-density region in qualitative agreement with that measured (Figs. 9C and 10B). The radiation pulse begins when the average radius is still between 3 and 5 mm (Fig. 12A), indicating a large spread in the plasma sheath thickness due to the instability growth. In the simulation, use of the nominal electron-photon coupling (denoted by E-RMHC:N in the figures) leads to the generation of slightly more radiation at the first compression than measured, and little internal energy is left over to initiate a significant re-expansion followed by a

https://doi.org/10.1017/S0263034601194036 Published online by Cambridge University Press

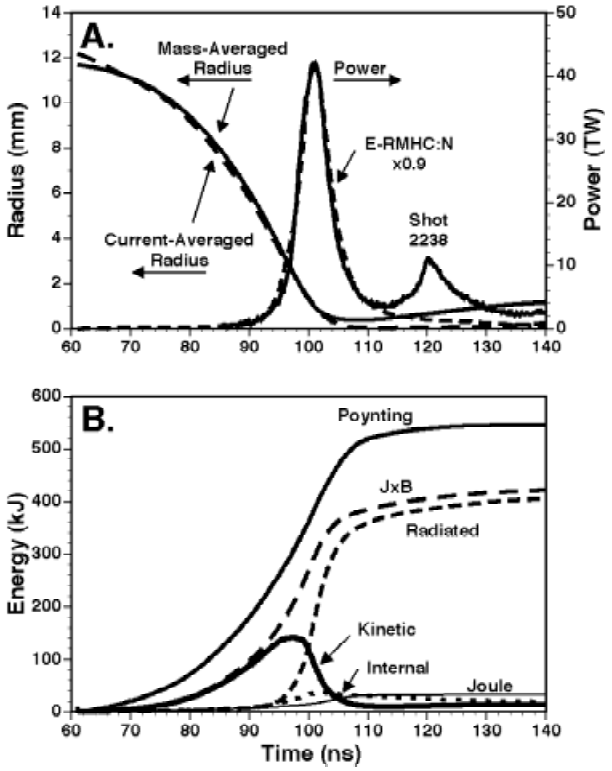

Fig. 12. (A) Mass-averaged radius (solid curve) and average-current (dashed curve) radius along with the radiation power (solid curve) for the E-RMHC:N simulation of a large-radius 0.84 mg implosion. (B) Associated energy flow.

second radial compression as observed. Reducing the coupling (denoted by E-RMHC:R in the figures), however, can lead to a second implosion in the simulation, as illustrated with the reduced-coupling simulation in Figures 9A and 9B.

Figure 12B shows the associated energy partition in the Figure 12A simulation using the nominal electron-photon coupling. The primary difference between this case and the case with the reduced electron-photon coupling (Fig. 9A, 9B) occurs in the internal energy, where the reduced coupling results in a higher internal energy. Both give similar radiation pulsewidths (Fig. 11 in Sanford *et al.*, 1998*c*). The energy deposited in the plasma comes primarily from the Lorentz ($\mathbf{J} \times \mathbf{B}$) force and goes primarily to accelerating the plasma, increasing the kinetic energy. Early in the process when instabilities have not become important and there has been little plasma heating, the energy deposited by the Lorentz force and plasma radial kinetic energies are essentially equal. Later, the instability destroys the plasma shell, accelerating plasma to the axis where it stagnates, and the kinetic energy diverges significantly from that generated by the Lorentz force. When stagnation begins, the internal energy starts to rise and the plasma begins to radiate. At this time, most of the plasma extends over a significant radial region. Energy still flows into the load through the Poynting flux, and part of this flux continues to accelerate the plasma that has not stagnated. The radiation continues to rise as the main part of the plasma stagnates. Well after stagnation, the total radiated energy is nearly equal to that provided by the Lorentz force acting on the plasma (Fig. 12B). As plotted, the calculation shows only a small contribution from the Joule heating.

For the highly symmetric arrays being discussed here, X-ray images reveal a well-defined circular emission ring on the cathode surface (Fig. 13). The elliptical shape of the rings in the figure reflects the distortion introduced by the 35° viewing angle (Fig. 1). Between −9 and −7 ns in Figure 13, the rings move inward at an average rate of about 0.45 mm/ns, increasing to about 0.53 mm/ns between −7 and −4 ns. These measured velocities are similar to the 0-D-calculated implosion velocities of the array at the corresponding times, and the radii of the rings correlate with both the peaks of the mass and current profiles calculated by an E-RMHC simulation (see distributions shown below images of Fig. 13). The rings are thus conjectured to be from radiating plasma produced by either electron-current flow into the imploding plasma shell or an associated ion heating of the cathode surface.

In the Figure 13 simulation, the radially converging plasma precursor from instability bubble regions begins to stagnate on axis about 9 ns prior to peak emission, reaching electron temperatures of about 1 keV. This precursor becomes detectable in X-ray imaging just at this time (Fig. 13A). The Figure 13 images indicate that the precursor emission expands axially to fill the entire 20-mm anode-cathode gap by the time peak X-ray emission occurs. Lagrangian-RMHC simulations (Hammer *et al.*, 1996) that account for camera response and viewing angle show that the interaction of the stagnated precursor plasma with that of the inward moving shell generates the appearance of a hot inward-moving, luminescent, cylindrical shell (Sanford *et al.*, 1997*c*) like that imaged in Figure 13. These data, combined with the above conjecture, suggest that a large fraction of the imploding

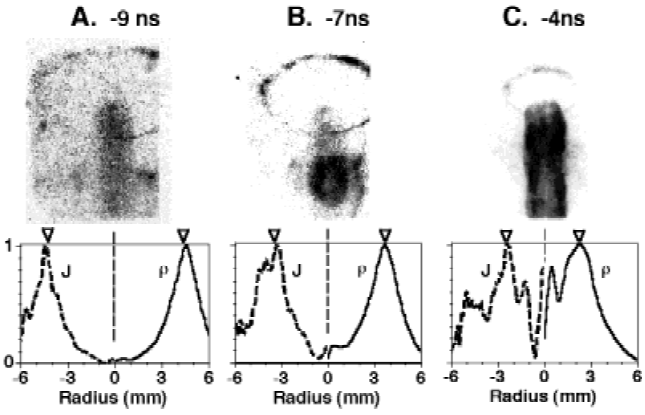

Fig. 13. Comparison of X-ray images (top) (sensitive to 0.2- to 0.3-keV and greater than 1-keV X rays) with E-RMHC:R simulations (bottom) of mass (solid curves) and current density (dashed curves), −9, −7, and −4 ns before peak power for a 1.3-mg large-radius array. Arrows correspond to RMS averages.

https://doi.org/10.1017/S0263034601194036 Published online by Cambridge University Press

mass is outside the emitting region and is either too cold or too diffuse to generate measurable X rays.

These observations are also consistent with 1-D RMHC analyses (Whitney *et al.*, 1997) that required a cool shell of plasma to implode onto a small amount of precursor plasma to explain the total to *K*-shell power ratio. In this model, the cool outer shell of plasma is needed to explain the greater than 4-to-1 power ratio measured, and it is also consistent with the spectral analysis (Sanford *et al.*, 1996*a*; Whitney *et al.*, 1997) which found that only 20% of the mass contributes to the *K*-shell radiation at the time of peak power. Moreover, the experimentally observed size of the *K*-shell emission region is smaller than the calculated mass-averaged plasma size (Figs. 9B and 13C), consistent with this low-mass fraction contributing to the *K*-shell emission.

3.3. Measured and simulated variation with array mass and radius

Following the 1995 wire number scan, two additional series of Saturn aluminum wire experiments were conducted in the high-wire-number, plasma-shell regime. These experiments were designed to better understand the conditions that optimize the total radiated power in this regime (Sanford *et al.*, 1997*b*). In the first series, the radius was held fixed at 12 mm and the mass was varied over the range 0.42 to 3.4 mg (Sanford *et al.*, 1998*c*). This series showed that when the mass of the array (which used ~192 wires) was reduced from above 1.9 to below 1.3 mg, a factor of 2 decrease in pulsewidth occurred (Fig. 14A), with an associated doubling of the peak total radiated power (Fig. 14B). In the second series, the array mass was held fixed near a value which maximized the peak power from the first series, and the array radius was varied (Sanford *et al.*, 1998*d*). This series showed that when the radius increased from 8.6 to 20 mm, for a mass of 0.6 mg in 136 wires, the total radiated pulsewidth (Fig. 14C) increased from only ~4 ns to ~7 ns and the associated peak total radiated power (Fig. 14D) remained relatively unchanged with radius.

Within the uncertainty of the electron-photon coupling approximation, the E-RMHC pulsewidths and total radiated peak power reasonably followed the measured trends (Fig. 14), using only a single value of a density perturbation seed set by the comparison in Figure 9A. Moreover, the simulations showed that over the mass- and radius-range measured, which spanned an implosion time of 40 ns to 90 ns, the shape of the simulated total-radiated-power pulse tracked the initial pulse measured. The implosion time of the simulated pulse agreed with that measured, within a shot-to-shot variation of only 2 ns. This agreement suggested that (100 ± 7)% of the initial mass was accelerated during the implosion, for these plasma-shell loads. The agreement in these comparisons that spanned an order of magnitude in load mass and almost a factor of 3 in array radius, and that use this single-value seed provided credibility to the average hydrodynamics of the E-RMHC simulations. These simulations showed that the R-T growth occurred via a two-staged process, if only 2-D effects were considered (Peterson *et al.*, 1998*a*, 1998*b*). The results also suggested that because in the radius scan the gap varied from 0.4 mm to 0.96 mm and because the simulation does not know about the discrete azimuthal nature of the array, the fact that the single seed described all the data implied that other asymmetries may be beginning to dominate these plasma-shell implosions.

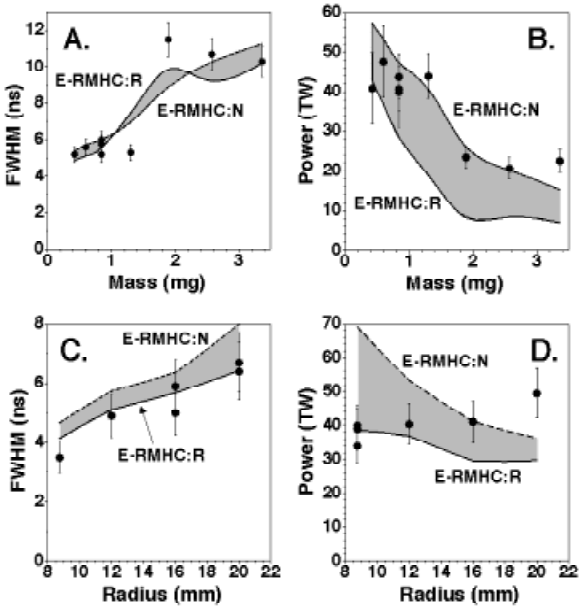

Fig. 14. Measured and E-RMHC simulated (A) total-radiated-power pulsewidth and (B) total radiated peak power as a function of mass, for the ~192-wire, large-radius mass scan. Measured and E-RMHC simulated (C) total-radiated-power pulsewidth and (D) total radiated peak power as a function of array radius, for the ~136-wire, mass = 0.6-mg radius scan.

The E-RMHC simulations attributed the decrease in pulsewidth and associated doubling of the peak total power as mass decreased to the faster implosion velocity of the plasma shell relative to the growth of the shell thickness. The data and modeling of the *K*-shell yields using either the Two-Level Model (Mosher *et al.*, 1998) or a phenomenological model (Thornhill *et al.*, 1996) showed the importance of maintaining sufficient kinetic energy per ion (that is, imploding sufficiently low-mass and high-velocity loads) if maximum yields are to be extracted. In contrast to the mass scan, the E-RMHC simulations correlated the decrease in pulsewidth with radius to the faster decrease of the shell thickness relative to the decrease in shell velocity. Importantly, the data showed that the improved uniformity provided by the large number of wires in the initial array reduced the effects of the R-T instability observed in small-wire-number, large-radius arrays (Deeney *et al.*, 1991, 1998*b*), and permitted the generation of high radiation powers from large-radius arrays for the first time. Large-radius arrays are often desired in order to optimize the energy transfer to the load, to reduce the electrical stress on the pulse forming lines feeding the load, or to provide the desired X-ray radi-

https://doi.org/10.1017/S0263034601194036 Published online by Cambridge University Press

ation characteristics as in Z (Spielman *et al.*, 1998). Little variation in *K*-shell yield was measured over the radial variation explored. In general, the variation in the measured *K*-shell yield with mass and radius was consistent with both the Two-Level Model and the phenomenological model with an ad hoc assumption on the radial convergence (Fig. 6B in Sanford *et al.*, 1998*c*, Fig. 10G in Sanford *et al.*, 1998*d*; Whitney *et al.*, 2001).

4. AXIAL OBSERVATIONS AT HIGH WIRE NUMBER

Owing to the greater number of radiative transitions available in tungsten relative to aluminum, tungsten wire loads are routinely used on Saturn and Z when maximum soft X-ray powers are desired. For this reason, the three *z*-pinch ICF concepts mentioned in the introduction all utilize the radiation generated from tungsten wires in the high-wire-number regime to heat high atomic number hohlraums. The absorbed radiation in the hohlraum is thermalized into a near Planckian X-ray source that would be suitable for imploding an ICF capsule if sufficient radiation temperature were attained. The extension of the observations and modeling discussed above to such tungsten loads on Saturn and Z can be found in Deeney *et al.* (1998*b*, 1998*c*, 1999), Lebedev *et al.* (2000), Peterson *et al.* (1998*a*, 1998*b*, 1999), Ruiz-Camancho *et al.* (1999), Sanford *et al.* (1998*b*), and Spielman *et al.* (1997, 1998). Subsequent to the Saturn measurements, nesting of the arrays has been found to mitigate the R-T development and has enabled additional power increases (40 ± 20%) with tungsten wire implosions on Z (Deeney *et al.*, 1998*a*). As with the extension to tungsten loads, the interested reader is here again directed to the original papers. Relevant to this review, however, is the reduction in radial size and associated azimuthal structure observed near stagnation that has recently been measured when nested tungsten arrays are imploded on foam targets. The measurements were made using the static-wall-hohlraum geometry (Fig. 15A). As such, they also serve as an example of the high temperatures that have been achieved in configurations needed for ICF studies with a *z* pinch (Fig. 15B).

The measurements were motivated by the need to understand the dynamics of the axial radiation that heats the hohlraum. In the single-sided X-ray drive of Figure 15B, the hohlraum is placed above a pulse-shaping target (PST) within an X-ray producing *z* pinch. In the two-sided X-ray drive of Figure 15C, the hohlraum is sandwiched between two PSTs. In either case, X rays produced in the PST enter the axial hohlraum through one or two REH (radiation entrance holes) and heat its walls. The X rays are generated in the PST by the thermalization of the kinetic energy, acquired when a cylindrical plasma shell created by one or more wire arrays collides with the PST. In this arrangement, the tungsten wires form an annular plasma radiation case (Sanford *et al.*, 1998*b*) by the time they strike the PST. The high-atomic-number radiation case traps a fraction of the X rays produced in the

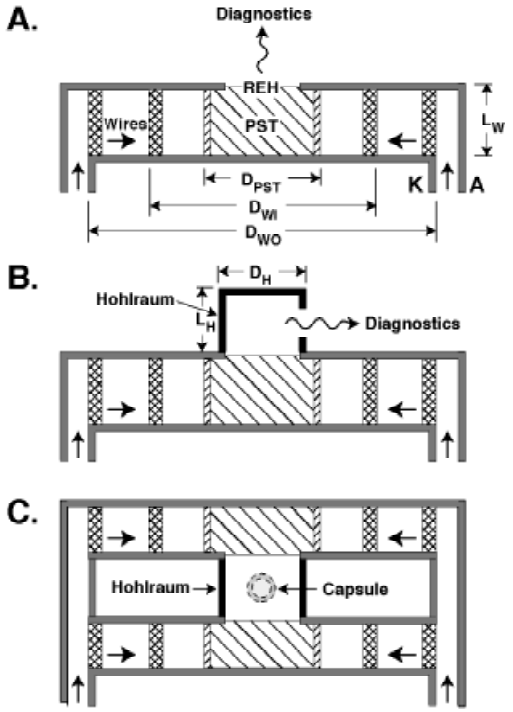

Fig. 15. Schematic of static-wall hohlraum geometry (A) without hohlraum, (B) for one-sided drive, and (C) for two-sided drive.

PST and radiation flows from the interior of the PST into the hohlraum, whose walls remain relatively static. A low-opacity foam fill is used in some of the PSTs so that as final stagnation is approached, the foam remains transparent to the X rays, yet provides a backpressure on the imploding mass. The backpressure enables additional energy to be extracted as the magnetic field compresses the PST. Changing the PST varies the X-ray pulse and the associated heating of the hohlraum. The single-sided drive of Figure 15B is that which has been tested to date and is associated with the measurements discussed here. The two-sided drive of Figure 15C is presently under development. It should permit both hotter and more spatially symmetric radiation fields to be produced within the hohlraum, where a capsule could be positioned with appropriate shine shields (Olson *et al.*, 1999).

The radiation entering the hohlraum is measured by diagnostics that view the source through the REH when the hohlraum is not present (Fig. 15A). Over the measured peak X-ray input powers *P* of 0.7 TW to 13 TW (obtained by varying the PST), the measured peak hohlraum temperature *T* scales as the Planckian relation $T \sim (P/A)^{1/4}$ (Fig. 16), and is in agreement with simple theoretical expectations (Sanford *et al.*, 2000*a*). *A* is the surface area of the hohlraum. In Figure 16, all the data except the highest temperature data of ~155 eV correspond to those measured with the NIF-scale hohlraum, which had a surface area of 153 mm^2 (Sanford *et al.*, 1999*d*). In Figure 16, the 85-eV drive simulates the ~10-ns foot pulse necessary for ICF ignition and propagation burn (Dittrich *et al.*, 1998; Wilson *et al.*, 1998) on the

https://doi.org/10.1017/S0263034601194036 Published online by Cambridge University Press

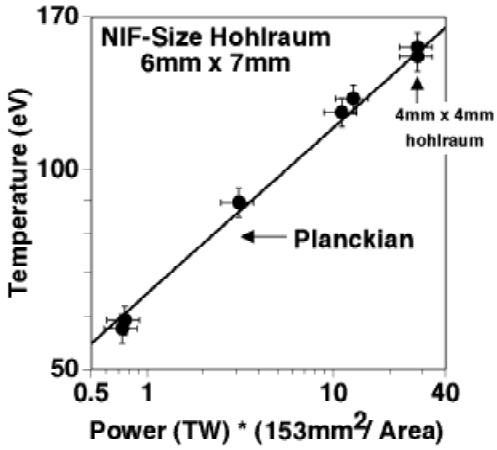

Fig. 16. Measured static-wall hohlraum temperature as a function of measured on-axis X-ray power. The Planckian is normalized by a calculation at 13 TW. 153 mm^2 corresponds to the surface area of the 6-mm × 7-mm hohlraum.

NIF. The 120-eV and ~155-eV temperatures correspond to those needed in the associated first- and second-drive steps (Sanford *et al.*, 2000*a*).

In the figure, the axial powers greater than a terawatt were achieved, in part, by removing the azimuthal asymmetries in the current return can and by using a nested array to mitigate the R-T instability. The use of a low-density (14 mg/cc) CH-foam PST decreased the effective radial size of the pinch at stagnation from ~2 to ~1 mm and permitted the same axial power to be produced through a 4-mm-diameter REH as was produced with a bare pinch through a 6-mm diameter REH (Fig. 17). The size reduction permitted the reduced-scale hohlraum to be heated with the same radiation power as that used to heat the NIF-scale hohlraum. Now, however, temperatures higher than those achievable in the NIF-scale hohlraum became possible because of the reduced surface area (Fig. 16). Such temperatures (~155 eV), especially when generated in a NIF-scale hohlraum heated by the symmetric drive geometry of Figure 15C, offer the opportunity to study the implosion of D_2-filled capsules capable of generating thermonuclear neutrons (Sanford *et al.*, 2000*a*). These studies would be useful for NIF-relevant neutron diagnostic development (Leeper *et al.*, 1997) and capsule fabrication performance evaluations (Wilson *et al.*, 2000).

The foam, like the inner shell of the nested array, appears to reduce the amplitude of the R-T instability. Associated with the radial size reduction, the width of the off-axis total radiated power pulse decreases by ~25% from 3.2 to 2.3 ns and the on-axis pulse from 5.2 to 4.0 ns. For either of the tight pinches plotted in Figure 17, periodic azimuthal structure is evident in the X-ray images of the REH. The structure is consistent with mode numbers of 4–8 (Fig. 18). Preliminary MHD simulations (N.F. Roderick, pers. comm.) with an imposed 5% density variation having sixfold symmetry on the outer array exhibit density variations with ~50% excursions near stagnation similar to the emission variations observed (Sanford & Roderick, 2001). In the simulations, the initial variation is amplified due to radial convergence. The posthole convolute structure on Z has a 12-fold azimuthal periodicity (Spielman *et al.*, 1998). Calculations of the current at the load indicate, however, that any variation in the current flowing in the load would be less than 1% (K.W. Struve, pers. comm.). The origin of such azimuthal mode structures in the emission images, when using such highly symmetric loads, is not yet understood.

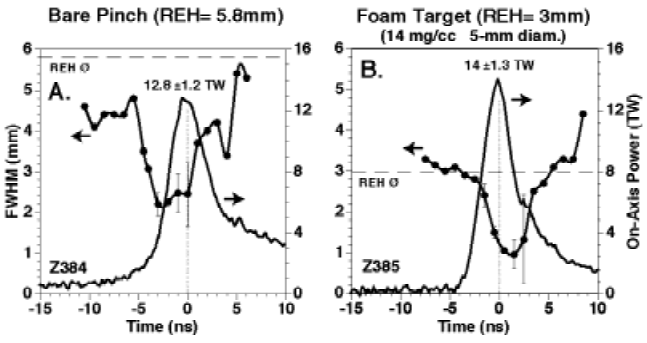

Fig. 17. Measured total radiation power and diameter (FWHM) of the X-ray emission from the REH of Figure 15A as a function of time (A) for a bare pinch, and (B) for a 5-mm diameter, 14 mg/cc CH PST. The diameters and masses of the nested array used were 35 mm and 2 mg/cc, and 17.5 mm and 1 mg/cc, with wire numbers of 240 and 120, respectively.

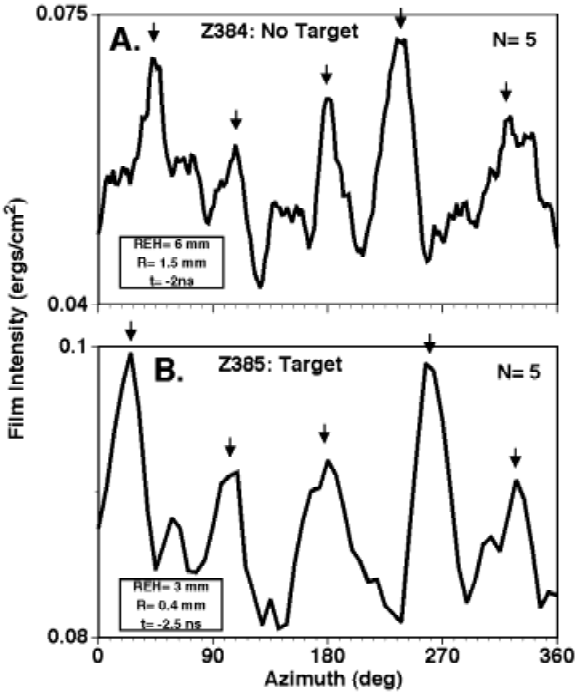

Fig. 18. Azimuthal lineout of X-ray images of the REH (A) associated with Figure 17A at a radius of 1.5 mm and 2 ns before peak REH emission, and (B) associated with Figure 17B at a radius of 0.4 mm and 2.5 ns before peak REH emission.

https://doi.org/10.1017/S0263034601194036 Published online by Cambridge University Press

5. SUMMARY

The 1995 Saturn experiments, where the wire number was systematically varied, demonstrated that a key parameter in significantly increasing radiation power and improving the quality of the pinch was the interwire gap spacing. When the gap decreased from 6 mm to 0.4 mm, the total radiated power increased by a factor of 20 and the energy by a factor of 2. On a linear scale, the data showed a dramatic increase in power below a gap of about 2 ± 0.6 mm. On a logarithm scale, the data indicated associated transitions near 2 mm in other measured radiation and pinch parameters. The transition near 2 mm correlated with a calculated transition in topology between that of individual wire plasmas at large gaps to that of a more uniform plasma shell at small gaps. Such a transition in topology has been recently observed in MAGPIE experiments (Lebedev *et al.*, 2000). For gaps less than 2 mm, the total radiated energy showed no change. The measured decrease in total radiated energy for gaps greater than ~2 mm was qualitatively consistent with the increased sensitivity to azimuthal variations in the wire plasma regime and the recently calculated transition in perturbation amplitude resulting from the development of the $m = 0$ instability in individual wires (Chittenden *et al.*, 2000). The azimuthal variations lead to a reduced efficiency for converting kinetic energy to thermal energy at stagnation, and the greater perturbation amplitude leads to increased coronal jetting and a softer implosion.

In contrast, the risetime showed no discontinuity near 2 mm, and scaled simply as the gap. Moreover, the order-of-magnitude increase in the power and its inverse gap dependence when normalized by the total radiated energy (Fig. 2) could not be explained by azimuthal asymmetries alone. RMHC simulations in the *r–z* plane, however, suggested that the measured change in peak X-ray power with gap (aside from the topology change effect) was related to the evolution of the thickness of a plasma shell due to the growth of axisymmetric R-T instabilities. In general, many features of the data and simulations as a function of gap were well summarized by the four-phase Heuristic Model (Haines, 1998). This model established the connection between the $m = 0$ perturbation in the individual wire plasmas (if they occurred when in an array) with the seed initiating the R-T instability in the *r–z* plane.

In the high wire number plasma-shell regime, the loads exhibited both a strong first and weaker second radiation pulse that correlated in time with a strong and then weaker radial convergence, hotter and then cooler electron temperatures of a radiating core, and higher and then lower ion velocities of the emitting plasma, as would be expected for a double implosion. At peak radiated power, which was associated with the first radial convergence, the pinch exhibited a hot core surrounded by a cooler plasma halo. The data through the first radial compression were well described by RMHC simulations in the *r–z* plane, such as those of Hammer *et al.* (1996) and Peterson *et al.* (1996), which included the evolution of an R-T instability in an axisymmetric implosion. In this regime, 1-D *K*-shell models such as those of Mosher *et al.* (1998) and Thornhill *et al.* (1996), which assume an ad hoc radial convergence, agreed with the measured *K*-shell yields as a function of mass and radius. Not yet included in any of the simulations, however, is an explanation of the azimuthal mode structure observed through the small REH (used for hohlraum heating in the static-wall configuration), when highly symmetric nested-array loads stagnate on axis.

Application of such high-wire-number loads at large radii has led to the heating of ICF relevant hohlraums to high temperature. In the single-sided static-wall-hohlraum (Olson *et al.*, 1999) configuration discussed here (Fig. 15B), temperatures of 130 ± 7 eV and 155 ± 8 eV have been achieved in NIF-scale and reduced-scale hohlraums, respectively. Extrapolating this concept with a NIF-scale hohlraum, using a single-feed double-sided driver (Fig. 15C), to a 50-MA generator, for example, is expected to provide conditions suitable for studying capsule implosions driven at peak temperatures of 240–270 eV (Sanford *et al.*, 1999d). Such generators are characteristic of the next generation Z-pinch drivers being considered (Struve *et al.*, 1999).

ACKNOWLEDGMENTS

The insights discussed in this review article were developed in close collaboration with the coauthors noted in the references. I would especially like to acknowledge both the productive and delightful interactions with Drs. John Greenly, John De Groot, Malcolm Haines, James Hammer, Barry Marder, Yitzhak Maron, David Mosher, Thomas Nash, Darrell Peterson, Norman Roderick, and Kenneth Whitney over the course of the *z*-pinch research, and with Drs. Ramon Leeper and Richard Olson during the recent hohlraum experiments. The Heuristic Model of Prof. Malcolm Haines reignited interest in understanding the fundamental mechanisms behind the X-ray power increase with wire number, and the interaction in the past few years with Drs. Jeremy Chittenden and Serge Lebedev in his group at Imperial College has added depth to the observations deduced from the original measurements. In a like fashion, the single-wire-expansion measurements by Drs. John Greenly, and Daniel Sinars in Prof. David Hammer's group at Cornell University, have provided new insights into the complexity of wire initiation, and gave credibility to the Saturn-implosion calculations of Dr. Jeremy Chittenden. The critical review of many of the papers embraced by this review provided by Dr. Keith Matzen increased the clarity of the presented analyses. Dr. Rick Spielman's early guidance in the installation of pinch loads on Saturn, Raymond Mock's meticulous attention to detail, Terry Gilliland's painstaking load installations, John McGurn's and Daniel Jobe's careful fielding of diagnostics, and Johann Seamen's leadership in overall assembly contributed in large part to the success of this research. Dr. Wendland Beezhold is particularly thanked for his vision in funding the 1995 experiments, and Drs. Donald Cook, Gerry Cooperstein, Jack Davis, Michael Jones, Ramon Leeper, John Maenchen, Keith Matzen, Dillon McDaniel, Jeffery Quintenz, Juan Ramirez, Auther Toor, and Gerry Yonas are thanked for their programmatic support that made this research possible. Lastly, Prof.

John De Groot, Dr. Richard Olson, and Teresa Cutler are thanked for their careful review of this manuscript.

Sandia is a multiprogram laboratory operated by the Sandia Corporation, a Lockheed Martin Company, for the U.S. Department of Energy under Contract No. DE-AC04-94AL85000.

REFERENCES

Beg, F.N. *et al.* (1997). *Plasma Phys. Fusion* **39**, 1.

Bloomquist, D.D. *et al.* (1987). In *Proc. Sixth Int. IEEE Pulsed Power Conf.*, Arlington, VA (Turchi, P.J. and Bernstein, B.H., Eds.), p. 310. New York: Institute of Electrical and Electronic Engineers.

Chittenden, J.P. *et al.* (1997). *Phys. Plasmas* **4**, 4309.

Chittenden, J.P. *et al.* (1999). *Phys. Rev. Lett.* **83**, 100.

Chittenden, J.P. *et al.* (2000). *Phys. Rev. E* **61**, 4370.

Cook, D.L. (1997). In *Eleventh IEEE Int. Pulsed Power Conf., Digest of Technical Papers* (Cooperstein, G. and Vitkovitsky, I., Eds.), p. 25. New York: Institute of Electrical and Electronic Engineers.

Cook, D.L. *et al.* (1998). In *Twelfth Int. Conf. on High-Power Part. Beams*, Haifa, Israel, June 7–12, 1998 (Markovits, M. & Shiloh, J., Eds.), p. 171. IEEE 98EX103.

Cuneo, M.E. *et al.* (1999). *Bull. Am. Phys. Soc.* **44**, 40.

Deeney, C. *et al.* (1991). *Phys. Rev. A* **44,** 6762.

Deeney, C. *et al.* (1997). *Phys. Rev. E*. **56**, 5945.

Deeney, C. *et al.* (1998*a*). *Phys. Rev. Lett.* **81**, 4883.

Deeney, C. *et al.* (1998*b*). *Phys. Plasmas* **5**, 2431.

Deeney, C. *et al.* (1998*c*). *Phys. Plasmas* **5**, 2605.

Deeney, C. *et al.* (1999). *Phys. Plasmas* **6**, 3576.

Dittrich, T.R. *et al.* (1998). *Phys. Plasmas* **5**, 3708.

Haines, M.G. (1998). *IEEE Trans. Plasma Sci*. **26**, 1275.

Haines, M.G. (2000). *Phys. Plasmas* **7**, 1672.

Haines, M.G. & A. Knight, Eds. (1993). *Third Int. Conf. on Dense Z Pinches*, London, UK, 1993, AIP Conference Proceedings 299, New York: American Institute of Physics.

Hammer, J.H. *et al.* (1996). *Phys. Plasmas* **3**, 2063.

Hurst, M.J. *et al.* (1999). *Rev. Sci. Instrum.* **70**, 468.

Kilkenney, J.D. *et al.* (1999). *Laser Part. Beams* **17**, 159.

Lash, J.S. *et al.* (1999). In *Inertial Fusion Sciences and Applications 99* (Hogan, W.J. and Tanaka, K.A., Eds.), p. 583. Paris: Elsevier.

Lebedev, S.V. *et al.* (1998). *Phys. Rev. Lett.* **81**, 4152.

Lebedev, S.V. *et al.* (1999). *Phys. Plasmas* **6**, 2016.

Lebedev, S.V. *et al.* (2000). *Phys. Rev. Lett*. **85**, 98.

Leeper, R.J. *et al.* (1997). *Rev. Sci. Instrum.* **68**, 868.

Leeper, R. J. *et al.* (1999). *Nucl. Fusion* **39**, 1283.

Marder, B.M. (1973). *Math. of Comp.* **29**, 434.

Marder, B.M. *et al.* (1998). *Phys. Plasmas* **5,** 2997.

Matzen. K.M. (1997). *Phys. Plasmas* **4**, 1519.

Matzen, K.M. (1999). *Fusion Engin. and Design* **44**, 287.

Matzen, K.M. *et al.* (1999). *Plasma Phys. and Controlled Fusion* **41**, A175–A184.

Mehlhorn, T.A. (1997). *IEEE Trans. Plasma. Sci.* **25**, 1336.

Michell, I.H. *et al.* (1996). *Rev. Sci. Instrum.* **67**, 1533.

Morse, R.L. & Carroll, D.E. (2000). *Bull. Am. Phys. Soc*. **45**, 788.

Mosher, D. (1989). In *Second Int. Conf. Dense Z-Pinches*, Laguna Beach, CA, AIP Conference Proceedings 195, pp. 191–200 (Pereira, N.R., Davis, J. and Rostoker, N., Eds.). New York: American Institute of Physics.

Mosher, D. (1994). *BEAMS '94, Proc. of Tenth Int. Conf. on High Power Part. Beams*, pp. 159–162. NTIS PB95-1443417. Springfield, Virginia: National Technical Information Service.

Mosher, D. & Colombant, D. (1992). *Phys. Rev. Lett.* **68**, 2600.

Mosher, D. *et al.* (1998). *IEEE Trans. Plasma Sci.* **26**, 1052.

Nash, T.J. *et al.* (1998). *J. Quant. Spectros. Radiat. Transfer* **60**, 97.

Nash, T.J. *et al.* (1999*a*). *Phys. Plasmas* **6**, 2023.

Nash, T.J. *et al.* (1999*b*). *Rev. Sci. Instrum.* **70**, 464.

Olson, R.E. *et al.* (1999). *Fusion Technol.* **35**, 260.

Pereira, N.R. & Davis, J. (1988). *J. Appl. Phys.* **64**, R1.

Pereira, N.R., Ed. (1989). In *Second Int. Conf. Dense Z Pinches*, Laguna Beach, CA, AIP Conference Proceedings 195, New York: American Institute of Physics.

Peterson, D.L. *et al.* (1996). *Phys. Plasmas* **3**, 368.

Peterson, D.L. *et al.* (1998*a*). In *Fourth Int. Conf. Dense Z Pinches*, Vancouver, Canada (Pereira, N.R., Davis, J. & Pulsifer, P.E., Eds.), pp. 201–210. New York: The American Institute of Physics.

Peterson, D.L. *et al.* (1998*b*). *Phys. Plasmas* **5**, 3302.

Peterson, D.L. *et al.* (1999). *Phys. Plasmas* **6**, 2178.

Porter, J.L. (1997). *Bull. Am. Phys. Soc*. **44**, 1948.

Quintenz, J.P. *et al.* (1996). In *Proc. of the Eleventh Int. Conf. on High-Power Part. Beams*, Prague, Czech Republic (Jungwirth, K. & Ullschmied, J., Eds.), p. 146. Academy of Sciences of the Czech Republic.

Quintenz, J.P. *et al.* (1998). In *BEAMS '98, Twelfth Int. Conf. on High-Power Part. Beams*, Haifa, Israel (Markovits, M. & Shiloh, J., Eds.), p. 9. IEEE 98EX103.

Ramirez, J.J. (1997). *IEEE Trans. Plasma Sci.* **25**, 155.

Reisman, D.B. (1998). Ph.D. Dissertation, University of California, Davis.

Ruggles, L.E. *et al.* (1995). *Rev. Sci. Instrum.* **66**, 712.

Ruiz-Camacho, J. *et al.* (1999). *Phys. Plasmas* **6**, 2579.

Ryutov, D.D. *et al.* (2000). *Rev. Mod. Phys.* **72**, 167.

Sanford, T.W.L. *et al.* (1995). *Bull. Am. Phys. Soc*. **40**, 1846.

Sanford, T.W.L. *et al.* (1996*a*). In *BEAMS '96, Proc. of the Eleventh Int. Conf. on High-Power Part. Beams*, Prague, Czech Republic (Jungwirth, K. and Ullschmied, J., Eds.), p. 146. Prague: Academy of Sciences of the Czech Republic.

Sanford, T.W.L. *et al.* (1996*b*). *Phys. Rev. Lett*. **77**, 5063.

Sanford, T.W.L. *et al.* (1997*a*). *Rev. Sci. Instrum*. **68**, 852.

Sanford, T.W.L. *et al.* (1997*b*). In *Fourth Int. Conf. Dense Z Pinches*, Vancouver, Canada (Pereira, N.R., Davis, J. and Pulsifer, P.E., Eds.), p. 561. New York: The American Institute of Physics.

Sanford, T.W.L. *et al.* (1997*c*). *Phys. Plasmas* **4**, 2188.

Sanford, T.W.L. *et al.* (1998*a*). In *BEAMS '98, Twelfth Int. Conf. on High-Power Part. Beams*, Haifa, Israel (Markovits, M. & Shiloh, J., Eds.), p. 229. IEEE 98EX103.

Sanford, T.W.L. *et al.* (1998*b*). *IEEE Trans. Plasma Sci.* **26**, 1086.

Sanford, T.W.L. *et al.* (1998*c*). *Phy. Plasmas* **5**, 3737.

Sanford, T.W.L. *et al.* (1998*d*). *Phys. Plasmas* **5**, 3755.

Sanford, T.W.L. *et al.* (1999*a*). *Phys. Plasmas* **6**,1270.

Sanford, T.W.L. *et al.* (1999*b*). *Phys. Plasmas* **6,** 2030.

Sanford, T.W.L. *et al.* (1999*c*). In *Inertial Fusion Sciences and Applications 99* (Hogan, W.J. and Tanaka, K.A., Eds.), p. 609. Paris: Elsevier.

Sanford, T.W.L. *et al.* (1999*d*). *Phys. Rev. Lett.* **83**, 5511.
Sanford, T.W.L. *et al.* (2000*a*). *Fusion Technol.* **38**, 11.
Sanford, T.W.L. *et al.* (2000*b*). *Phys. Plasmas* **7**, 4669.
Sanford, T.W.L. & Roderick, N.F. (2001). Submitted to *IEEE Trans. Plasma Sci.*
Sinars, D.B. *et al*. (2000). *Phys. Plasmas* **7**, 1555.
Sinars, D.B. *et al*. (2001). *Phys. Plasmas* **8**, 216.
Spielman, R.B. *et al.* (1993). In *Third Int. Conf. Dense Z Pinches*, London, UK, AIP Conference Proceedings 299, pp. 404–420. (Haines, H. and Knight, A., Eds.). New York: American Institute of Physics.
Spielman, R.B. *et al.* (1996). In *BEAMS '96, Proc. of the Eleventh Int. Conf. on High-Power Particle Beams*, Prague, Czech Republic (Jungwirth, K. and Ullschmied, J., Eds.), p. 150. Prague: Academy of Sciences of the Czech Republic.
Spielman, R.B. *et al.* (1997). In *Fourth Int. Conf. Dense Z Pinches*, Vancouver, Canada (Pereira, N.R., Davis, J. and Pulsifer, P.E., Eds.), p. 101. New York: The American Institute of Physics.
Spielman, R.B. *et al.* (1998). *Phys. Plasmas* **5**, 2105.
Struve, K.W. *et al.* (1999). In *Proc. of the Twelfth Int. Pulsed Power Conf.*, Monterey, CA (Stallings, C. & Kirbie, H., Eds.), p. 493. New York: Institute of Electrical and Electronic Engineers.
Thornhill, J.W. *et al.* (1996). *J. Appl. Phys*. **80**, 710.
Whitney, K.G. *et al.* (1997). *Phys. Rev. E* **56**, 3540.
Whitney, K.G. *et al.* (2001). *Phys. Plasmas* **8**, 3708.
Wilson, D.C. *et al.* (1998). *Phys. Plasmas* **5**, 1953.
Wilson, D.C. *et al.* (2000). *Fusion Technol.* **38**, 16.
Yonas, G. (1998). *Sci. Am.* **279**, 40.

https://doi.org/10.1017/S0263034601194036 Published online by Cambridge University Press